JMEPEG (2019) 28:4918–4930
https://doi.org/10.1007/s11665-019-04256-z

1059-9495/$19.00

Molecular Dynamics Simulation Study of Uniaxial Ratcheting Behaviors for Ultrafine-Grained Nanocrystalline Nickel

Snehanshu Pal, Karanam Gururaj, Md. Meraj, and Ravindra Giriraj Bharadwaj

(Submitted June 12, 2018; in revised form June 23, 2019; published online August 7, 2019)

In this paper, molecular dynamics (MD) simulation-based study of deformation behavior of ultrafine-grained nanocrystalline nickel under asymmetric cyclic loading having stress ratios (*R*) such as − 0.2, − 0.4 and − 0.6 for different temperatures, viz. 100, 300 and 500 K, has been performed using embedded atom method potential. The predicted ratcheting strain by MD simulation for nanocrystalline Ni varies from 15 to 30%. A significant increase in ratcheting strain has been observed with the increase in temperature. It has been observed that the number of vacancies increases, and the number of clusters decreases with the increase in temperature. Slight reduction in crystallinity is identified at the middle of the each loading cycle from the performed cluster analysis. Zigzag pattern of dislocation density has been observed and leads to the decrease in dislocation density with the increase in temperature. Stress ratio does not show any significant effect on the number of vacancies, clusters and dislocation density on structural evolution during the asymmetric cyclic loading. Slight change in the grain rotation has been observed with the increase in temperature, and there is almost no change in the final texture evolved. From the post-tensile tests, ultimate tensile strength that remains same may be due to constant average dislocation density.

Keywords molecular dynamics, nanocrystalline, ratcheting, stress ratio

1. Introduction

Nanocrystalline (NC) materials have been subject of great interest in recent years because of their unique mechanical, electrical, optical and electronic properties (Ref 1, 2). NC materials usually have less than 100 nm grain size having large volume fraction of grain boundary compared to coarse-grained crystalline materials. They are used in structural applications because of their excellent mechanical properties as the large volume fraction of grain boundaries hinders the movement of dislocations (i.e., dislocation pileup is occurred) and back stress is built up, which is responsible for enhancement of strength (Ref 3-6). Thus, ultimate tensile strength (UTS) for ultrafine-grained nanocrystalline is found to exhibit higher strength in the order of GPa unit. On the other hand, UTS for coarse-grained polycrystalline materials exhibits lower strength in the order of MPa unit. This is because coarse-grained polycrystalline materials have less volume fraction of grain boundary compared to NC materials and accordingly back stress because dislocation pileup is not so high in the case of coarse-grained polycrystalline materials. In this juncture, it is pertinent to mention that in the case of monocrystals, UTS is generally very high as defects are absent in perfect monocrystal specimens.

Deformation of NC materials is mainly controlled by grain boundary-mediated mechanisms like grain boundary sliding, grain rotations, grain boundary migration (Ref 7-11). In structural applications, whenever the materials are subjected to deformation under static or cyclic loadings due to compression and tension cycles, there will be continuous accommodation of plastic strain and it eventually causes the fatigue failure of material. In this perspective, NC materials may be effective alternative as they have good fatigue resistance because of their high volume fraction of grain boundary, which hinders the movement of crack (Ref 12). Several researchers have reported that deformation behavior of nanocrystalline metallic system changes over from dislocation-controlled plasticity to grain boundary-mediated plasticity like grain boundary sliding and grain rotation with the decrease in grain size (Ref 13-15). Since grain boundary network consists of high density of dislocations in NC regime which is difficult to characterize, several atomistic simulations are performed to track the structural evolution of network of grain boundary during the deformation of NC metals (Ref 16, 17). Hanlon reported that pure NC Ni fatigue resistance increases because of grain refinement and hardens during cyclic loading over a range of fatigue conditions (Ref 18). Along with conventional fatigue, deformation under asymmetric cyclic loading or ratcheting behavior is also identified as one of the common ways of material failure and has also been dominant area of research over past few decades (Ref 19-24). In the case of ratcheting deformation, if there is

Electronic supplementary material The online version of this article (https://doi.org/10.1007/s11665-019-04256-z) contains supplementary material, which is available to authorized users.

Snehanshu Pal and **Karanam Gururaj**, Department of Metallurgical and Materials Engineering, National Institute of Technology Rourkela, Rourkela 769008, India; **Md. Meraj**, Department of Metallurgical and Materials Engineering, National Institute of Technology Rourkela, Rourkela 769008, India; and Department of Mechanical Engineering, G H Raisoni Academy of Engineering and Technology, Nagpur 440016, India; and **Ravindra Giriraj Bharadwaj**, Department of Mechanical Engineering, University of California Riverside, Riverside, CA 92521. Contact e-mail: pals@nitrkl.ac.in.

sufficient high stress to cause yielding, there will be cyclic accumulation of plastic strain under nonzero mean stress and it accelerates the process of deformation after each and every cycle resulting in early failure of component compared to conventional fatigue (Ref 25, 26). Controlling parameters like stress ratio, stress amplitudes, temperature, microstructure influence significantly accumulated strain during asymmetric cyclic loading (Ref 20, 23, 27). Temperature is one of the key parameters which influence the process of ratcheting as it causes the reduction in flow stress resulting in further deformation when the material is used at high service temperature (Ref 28). Many experimental studies have been performed on cyclic behavior of nanocrystalline metallic system; however, performing fatigue experiments at high temperatures is very costly and time-consuming. Experiments give two-dimensional view of microstructure, but grain rotation and sliding are linked with three-dimensional view and it is very difficult to track the structural evolution of each grain at nanoscale (Ref 29). In this regard for a better understanding of cyclic behavior, molecular dynamics (MD) acts as powerful and effective tool for providing atomic-level understanding of structural evolution and underlying deformation mechanism during ratcheting. Schiøtz has performed molecular dynamics (MD) simulations on nanocrystalline Cu and reported that mobility of grain boundaries increases during the cyclic loading resulting in coarsening of grains (Ref 30). Farkas et al. (Ref 31) have reported the formation of nanovoids in NC Ni at grain boundary from two or more dislocations, whenever dislocations cannot cross the grain boundary during ratcheting. According to Rupert and Schuh (Ref 32), grain boundaries get relaxed during cyclic loading for small amounts of plastic deformation and become stronger by having equilibrium grain boundary structure or low energy configurations, which results in cyclic hardening of material. Several MD simulation-based investigations have been performed on fatigue behavior of materials (Ref 30, 33); however, there are few reports that are related to asymmetric loading conditions (Ref 28). Moser et al. (Ref 34) have investigated deformation behavior during cyclic loading and reported cyclic hardening occurs during the initial stages of deformation in NC Ni. There is no literature available detailing the ratcheting behavior of NC metals and its associated atomic-level underlying mechanism. At this juncture, it is worth mentioning that the study of atomic-scale deformation mechanism is necessary to get thorough understanding of ratcheting behavior of nanocrystalline metallic system. The aim of this investigation is to study the structural evolution and underlying deformation mechanism of ultrafine-grained NC Ni under asymmetric cyclic loading condition. In this work, ratcheting deformation simulations have been performed for six cycles to understand the nature of strain accumulation in ultrafine-grained nanocrystalline nickel for different stress ratios ($R = -0.2, -0.4, -0.6$) at different temperatures, viz. 100, 300, 500 K. In addition, the effect of ratcheting on specimen stress–strain behavior is investigated by performing simulated tensile tests before and after ratcheting deformation.

2. Molecular Dynamics Simulation Model

Three-dimensional nanocrystalline (NC) Ni specimen has been prepared using Voronoi method (Ref 35) in AtomEye software (Ref 36) and is presented in Fig. 1(a) [colored according to centrosymmetry parameter (CSP)]. The complete specimen contains 27 uniform grains (grain size $\sim$ 5 nm) having random orientations. A 14 nm $\times$ 14 nm $\times$ 14 nm simulation box is taken for performing molecular dynamics (MD) simulation, and the simulation box contains 253,505 atoms. The specimen is equilibrated using the conjugate gradient algorithm through local energy minimum for 100 ps. Time step of 2 fs is taken, and periodic boundary conditions are applied in three directions for performing all the ratcheting simulations. The specimens are subjected to uniaxial tensile and uniaxial asymmetric cyclic loading along the *Y*-direction [010], and the simulated tests are performed for three different temperatures, namely 100, 300 and 500 K. The tensile test is carried out at strain rate of 10^8 s^{-1}. In this paper, engineering stress–strain plots are taken for studying the deformation of NC Ni. Engineering stress is defined as the applied load on test specimen divided by the initial cross-sectional area of a specimen, engineering strain is the change in length during deformation divided by the initial length of a specimen, and ultimate tensile strength is the maximum tensile stress which can be withstand by a materials during deformation (Ref 37-40). All the simulations are performed using NVE ensemble integrated with velocity Verlet algorithm. Ratcheting simulations have been carried out under various stress ratios (R) (e.g., -0.2, -0.4 and -0.6) and temperatures (e.g., 100, 300 and 500 K). Stress ratio (R) is defined as the ratio of the minimum stress (σ_{min}) to the maximum stress (σ_{max}), and in the present simulation σ_{max} is chosen as 90% of UTS of pure NC Ni at respective temperatures during ratcheting. During the simulation, the stress value increased from zero to the maximum stress (σ_{max}) by having step size as $\delta d_1 = \sigma_{max}/5$ in five steps and decreased to zero in the same way. Similarly, the minimum stress having step size as $\delta d_2 = \sigma_{min}/5$ in five steps and obtained step size is used to complete the loading cycle. For each loading cycle, stress is varied in 20 steps and is continued for 6 cycles. In the present simulation, the maximum stress (σ_{max}) is fixed, and from stress ratios (R) corresponding values of the minimum stress (σ_{min}) have been obtained. Here, Berendsen barostat method (Ref 41) has been applied for applying stress (in the form of pressure) on specimen. The R values have been chosen in such a manner that all the simulation cases comprise positive mean stress conditions.

In this study, ratcheting strain has been calculated as:

$$\text{Ratcheting strain}\% = \left[\frac{(Y_{hi} + Y_{lo}) - L}{2L}\right] * 100 \qquad \text{(Eq 1)}$$

where Y_{hi} and Y_{lo} are the elongated crystal coordinates in the positive and negative y-direction, respectively, and L is the initial length of the crystal in the y-direction.

All the atomistic calculations are executed using a large-scale atomic/molecular massively parallel simulator (LAMMPS) (Ref 42) with EAM FS (embedded atom model Finnis–Sinclair) potential developed by Mendelev et al. (Ref 43) applicable for Ni systems. As per the Finnis/Sinclair model, the total energy E of the crystal is expressed as follows:

$$E = \frac{1}{2}\sum_{i,j,i\neq j}\phi_{ij}(r_{ij}) + \sum_{i}F_i(\rho_i) \qquad \text{(Eq 2)}$$

where ϕ_{ij} represents the paired energy between atoms i and j separated by a distance r_{ij} and F_i is the embedding energy associated with embedding an atom i into a local site with an

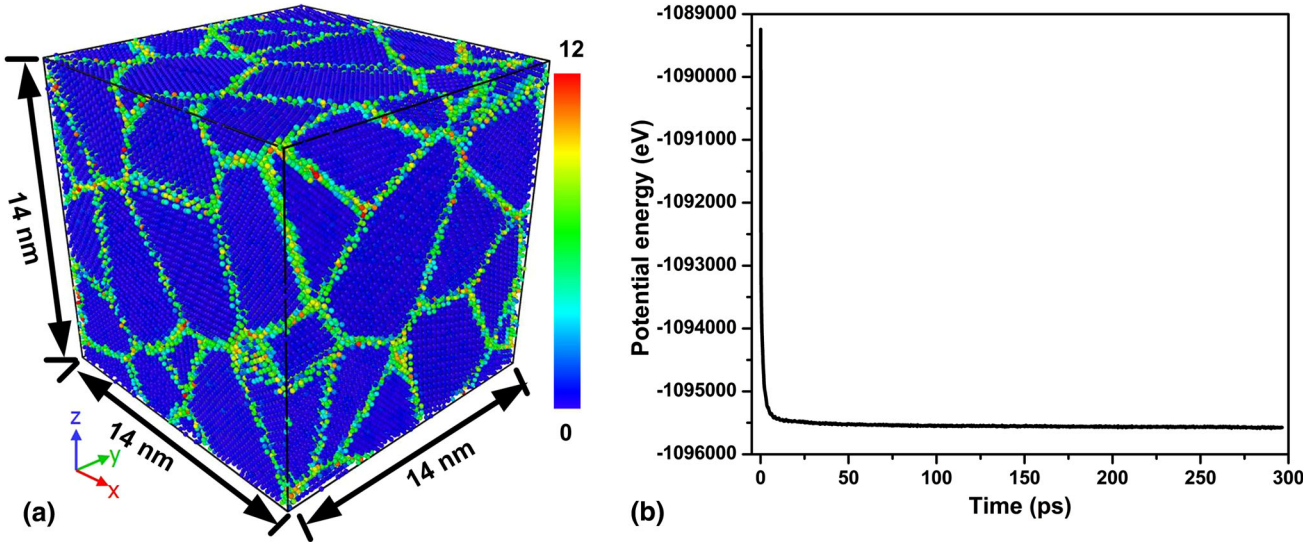

Fig. 1 (a) Three-dimensional snapshots of NC Ni specimen and (b) plot of potential energy with respect to time

electron density ρ_i. The electron density is calculated using the following equation:

$$\rho_i = \sum_{j,j\neq i} f_j(r_{ij}) \quad \text{(Eq 3)}$$

where $f_j(r_{ij})$ is the electron density at the site of atom i arising from atom j at a distance of r_{ij} and the generalized elemental potentials are written as follows:

$$\phi(r) = \frac{A\exp[-\alpha(r/r_e - 1)]}{1 + (r/r_e - k)^{20}} - \frac{B\exp[-\beta(r/r_e - 1)]}{1 + (r/r_e - \lambda)^{20}} \quad \text{(Eq 4)}$$

where r_e is the equilibrium spacing between the nearest neighbors. A, B, α and β are the adjustable parameters, whereas k and λ are two additional parameters for the cutoff. The electron density function is expressed as:

$$f(r) = \frac{f_e\exp[-\beta(r/r_e - 1)}{1 + (r/r_e - \lambda)^{20}} \quad \text{(Eq 5)}$$

Potential energy versus time graph along with atomic snapshots is shown in Fig. 1(b). This plot is calculated using the conjugate gradient algorithm to minimize the potential energy. The conjugate gradient algorithm (CGA) is one of the significant methods to look for a local minimum. CGA is not only specific for atomistic simulations; function $V(r)$ can be used for any N-dimensional function $f(x)$ which is a well-defined gradient. In the case of atomistic simulations, there are significant features that can be employed to optimize the algorithm at the possible expense of generalization. It is observed from Fig. 1(b) that potential energy is sharply decreased, and after few ps, it becomes constant with the increasing simulation time.

Dislocation density (Ref 44, 45) is taken as the sum of all dislocation lengths per unit volume of the specimen, i.e.,

$$\text{Dislocation density} = \frac{\text{sum of all dislocation length}}{\text{volume of the specimen}} \quad \text{(Eq 6)}$$

Wigner–Seitz defect analysis (Ref 46, 47) is used to count vacancies at different stages of simulated uniaxial ratcheting cycle. This analysis tool effectively identifies point defects using Wigner–Seitz cell method. The Wigner–Seitz cell method actually checks the defective state of the crystal structure with respect to the reference state, which is a perfect crystal lattice. Wigner–Seitz defect analysis identifies the position of the displaced atom by comparing with perfect crystal structure taken as a reference. In this method, if some sites are found to be occupied by zero atoms, the identified defect is vacancy. On the other hand, if some sites are found to be occupied by more than one atom, the detected defect is interstitials.

Centrosymmetry parameter (CSP) analysis is used to analyze the atomic strain evolution during the uniaxial cyclic loading. The CSP (Ref 48) can be defined as follows:

$$\text{CSP} = \sum_{i=1,6} \left|R_i + R_{i+N/2}\right|^2 \quad \text{(Eq 7)}$$

where R_i and $R_{i+N/2}$ are the vectors or bonds from the central atom to the six pairs of opposite nearest neighbors in the FCC lattice. The CSP value is zero for perfect FCC lattice under the homogeneous elastic deformation, where each atom is surrounded with a pair of equal and opposite bonds with nearest neighbors, and it increases toward positive values with the increase in defects where the surrounded bonds change its direction and/or length.

The radial distribution function (RDF) analysis is an effective tool for determining the local structure of the specimen. RDF ($g(r)$) is actually the probability of finding a neighbor atom at a distance r away from a central atom, which is expressed by the following relation (Ref 49):

$$g(r) = \frac{V}{N^2}\left\langle \sum_{i=1}^{N} \frac{n(r)}{4\pi r^2 \Delta r} \right\rangle \quad \text{(Eq 8)}$$

where V denotes the total volume of the system, N is the number of atoms and $n(r)$ is the number of particles found at a distance between r and $r + \Delta r$. Common neighbor analysis (CAN) is obtained by the decomposition of the RDF plots, whereas to determine the CNA, decomposed RDF function is expressed by the following equation (Ref 50):

$$g(r) = \sum_{jkl} g_{jkl}(r) \quad \text{(Eq 9)}$$

Atomic configuration snapshots capturing CSP analysis, RDF, cluster analysis, Wigner–Seitz defect analysis and dislocation extraction have been performed using OVITO (Ref 51). Grain tracking algorithm (GTA) is the post-processing method which is used to convert the positions of the atoms in the simulation into structural measurements (Ref 29, 30, 52). In the present simulation, grain tracking algorithm (GTA) is used track the orientation of grains using CSP and atomic positions as required inputs. CSP gives information about the local distortion using the position of atoms which is used to differentiate between crystalline atoms from GB (Ref 53). GTA tracks orientation of each crystal at each atomic position by considering neighboring atoms using FCC as reference. By using misorientation angle as low angle grain boundary fixed, algorithm tracks local orientation at each atomic position within grain. From this, by calculating the average of all local orientations within grain the orientation of grain can be found and grain structure can be visualized. The orientation of each grain and the overall specimen texture are visualized with pole figures and inverse pole figures.

The main characterization of grain boundary motion parameters in MD simulation consists of the calculation of local properties of each atom, such as energy, stress or local lattice distortion, and qualitative observations, such as the migration of a certain grain boundary, GB sliding or the rotation of a specific grain (Ref 53). However, grain rotation in nanocrystalline specimen during deformation process occurs as the mechanism of the energy reduction in the system (Ref 29).

3. Results and Discussion

Molecular dynamics (MD) simulations of uniaxial ratcheting at various temperatures (e.g., 100, 300 and 500 K) and equivalent stress values (equal percentage of ultimate tensile strength of corresponding temperature) have been performed for NC Ni specimen in this study. Firstly, therefore MD simulations have been carried out to evaluate stress–strain behavior of the NC Ni at various temperatures (100, 300 and 500 K) and to select the maximum loading conditions for ratcheting and the obtained stress–strain curves are presented in Fig. 2(a). The tensile strength of pure NC Ni increases maximum up to 3.5, 2.98, 2.35 GPa at different temperatures, viz. 100, 300, 500 K, respectively. The magnitude of ultimate tensile strength is found to be decreased with the increasing temperature. This is owing to occurrence of flow softening of NC Ni at high temperature. This indicates mechanical properties of NC Ni are temperature sensitive, which necessitates the study of ratcheting behavior of this system for different temperatures. The uniaxial ratcheting simulation has been performed here taking the maximum tensile load (σ_{max}) is equal to 90% of the ultimate tensile strength (UTS) value of the NC Ni at the corresponding temperature. The minimum stress (σ_{min}) values applied as a compressive load are varied as per the chosen stress ratios (e.g., − 0.2, − 0.4 and − 0.6) for ratcheting simulation. The combinations of the adopted σ_{max} and σ_{min} values for each simulation are listed in Table 1. A comparative analysis of MD simulation and real experimental true stress–true strain curves of NC Ni specimen at room temperature is shown in Fig. 2(b). From both experimental (Ref 54) and simulation methods in nanoscale, the variation in results is less.

Representative applied loading (stress) cycles for different temperatures (e.g., 100, 300 and 500 K) at specific $R = -0.6$ and corresponding resulted strain cycles are shown in Fig. 2(c) and (d), respectively. Local fluctuation in strain plots during asymmetric cyclic loading is observed, but overall trend of strain curve is at par with the applied loading cycles. Accumulation of ratcheting strain is known to occur for such types of cases during asymmetric stress-controlled cyclic loading with nonzero mean stress.

Figure 3(a) shows the true stress–true strain curves for NC Ni at various temperatures. It is observed that the yield stress, ultimate tensile strength and flow stress decreased with the increasing temperature. It indicates that softening phenomenon is happened during deformation. It can be seen that a saw tooth shape nature of true stress–strain curves for NC Ni is observed under tensile deformation after the yield stress and it is found to be more at 100 K than 300 and 500 K temperatures. This type of observation is happened in stress–strain curves due to the phenomena of dislocation nucleation and movement, formation of dislocation junctions and dislocation annihilation (Ref 55). Figure 3(b) shows the dislocation density versus true strain plots at various temperatures under uniaxial tensile deformation condition. It is found that curve of dislocation density versus true strain is shifted toward upward with the decreasing temperature under uniaxial tensile test. It is due to the softening phenomenon which increases with the increasing temperature. In the plots of dislocation density, zigzag lines are observed during tensile deformation. It indicates the dislocation nucleation and annihilation during deformation of NC Ni. Figure 3(c) shows the inverse pole figures for NC Ni under uniaxial tensile deformation at three different temperatures. The stereographic projections along Z-direction to show the evolution of the orientations of overall random texture distribution of all grains during uniaxial tensile deformation are investigated here. Inverse pole figures are assisted to evaluate the grain rotation during deformation. It is observed from inverse pole figures that grain rotations during uniaxial tensile deformation increased with the increasing testing temperature. Figure 3(d) shows the pole figures' distribution of grain orientation {111} type pole for three different temperatures at the 40% of true strains under tensile deformation condition. The overall random texture distribution of pole figure in the specimens at different temperatures is investigated during uniaxial tensile deformations. It can be seen from Fig. 3(d) that the total number of poles projected at 300 K temperature is observed to be more compared to 100 and 500 K temperatures.

To show the ratcheting strain is a function of temperature, uniaxial ratcheting simulations have been performed at three different temperatures, viz. 100, 300 and 500 K. The variation in ratcheting strain with the number of cycles at different temperatures at specific stress ratios is presented in Fig. 4(a), (b) and (c). It has been observed that with the increase in temperature there is a significant increase in ratcheting strain as the increase in temperature takes the advantage of having lower flow stress required for the further deformation which indicates that materials exhibit softening behavior at high temperature. It can be inferred from the above discussion that ratcheting strain strongly depends on temperature. Figure 4(d), (e) and (f) shows the relationship between the ratcheting strains with the number

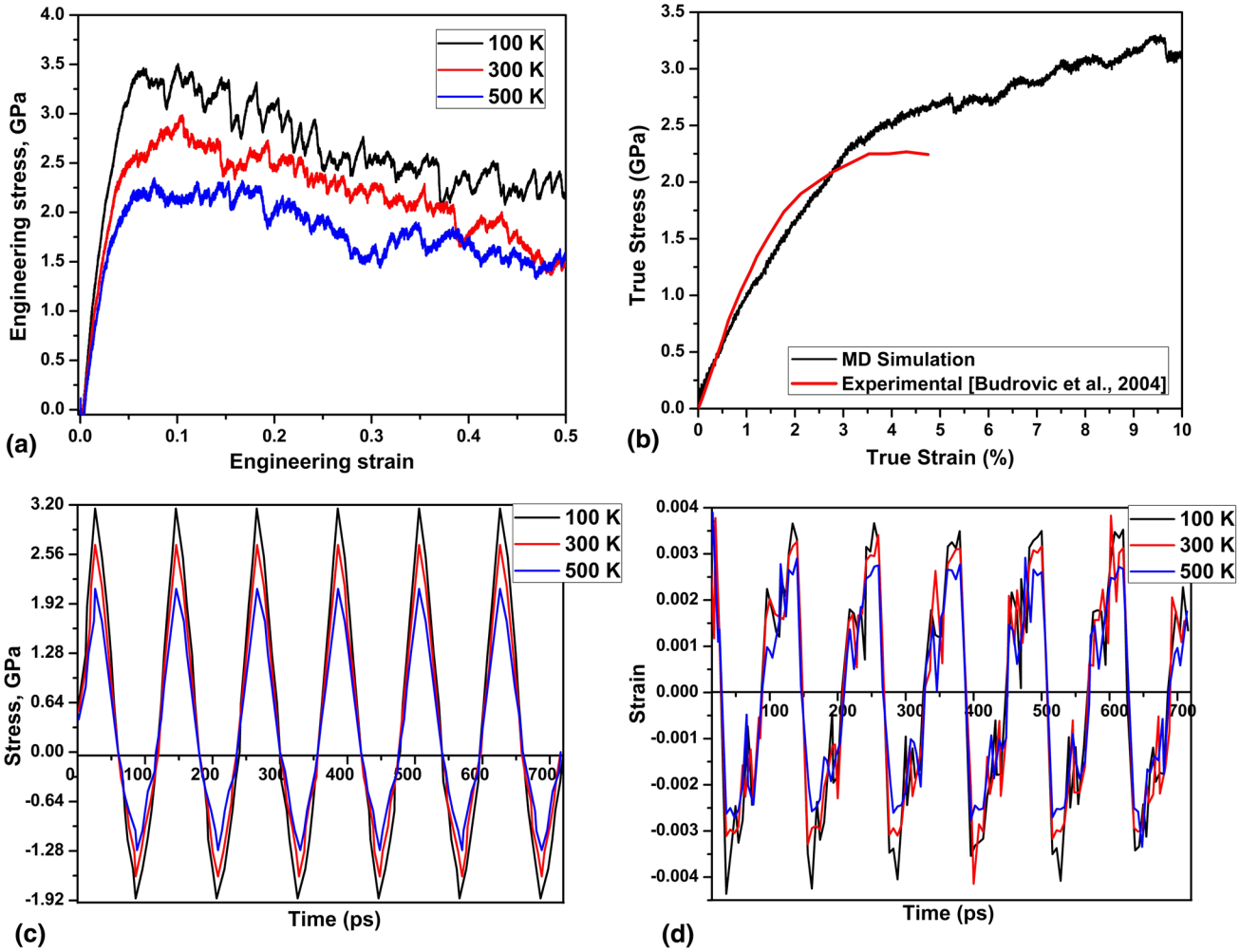

Fig. 2 (a) Engineering tensile stress–strain curves at various temperatures, (b) a comparative study of MD simulation and real experimental true stress–true strain curves of nanocrystalline Ni specimen at room temperature. [Experimental result is taken from the literature (Budrovic et al. (Ref 53))], (c) stress vs. time plots for different temperatures at stress ratio (R) = − 0.6 and (d) strain vs. time plots for different temperatures at stress ratio (R) = − 0.6

Table 1 Input parameters of NC Ni for the asymmetric cyclic loading simulations

	Temperature								
	100 K			300 K			500 K		
R	UTS (GPa)	σ_{max} (GPa)	σ_{min} (GPa)	UTS (GPa)	σ_{max} (GPa)	σ_{min} (GPa)	UTS (GPa)	σ_{max} (GPa)	σ_{min} (GPa)
− 0.2	3.5	− 3.15	0.63	2.98	− 2.68	0.54	2.35	− 2.11	0.42
− 0.4	3.5	− 3.15	1.26	2.98	− 2.68	1.07	2.35	− 2.11	0.84
− 0.6	3.5	− 3.15	1.89	2.98	− 2.68	1.61	2.35	− 2.11	1.27

of cycles at different stress ratios during the asymmetric cyclic loading. Ratcheting strain increases abruptly for the first two cycles of loading and becomes steady with minor fluctuations for remaining cycles of loading at different temperatures. It is observed from Fig. 4 that ratcheting strain predicted by MD simulation for NC Ni varies from 15 to 30%. It has also been observed that with the increase in magnitude of stress ratio (R), the minimum stress (σ_{min}) in amplitude increases resulting in greater allowable strain in the material (refer to Fig. 4d, e and f). Accumulative ratcheting strain decreased with the increasing compressive stress within a cycle. Earlier investigation performed by Kang et al. (Ref 27) showed that strain accumulation in sample versus the number of cycles takes place in 3 stages: initial sharp increase in accumulation of strain, maintains steady state and finally the increase in strain leads to failure of sample which is analogous to creep curves. However, in the present simulation only two stages are appeared as the simulation is carried only up to 6 cycles and is not carried out till failure of the specimen.

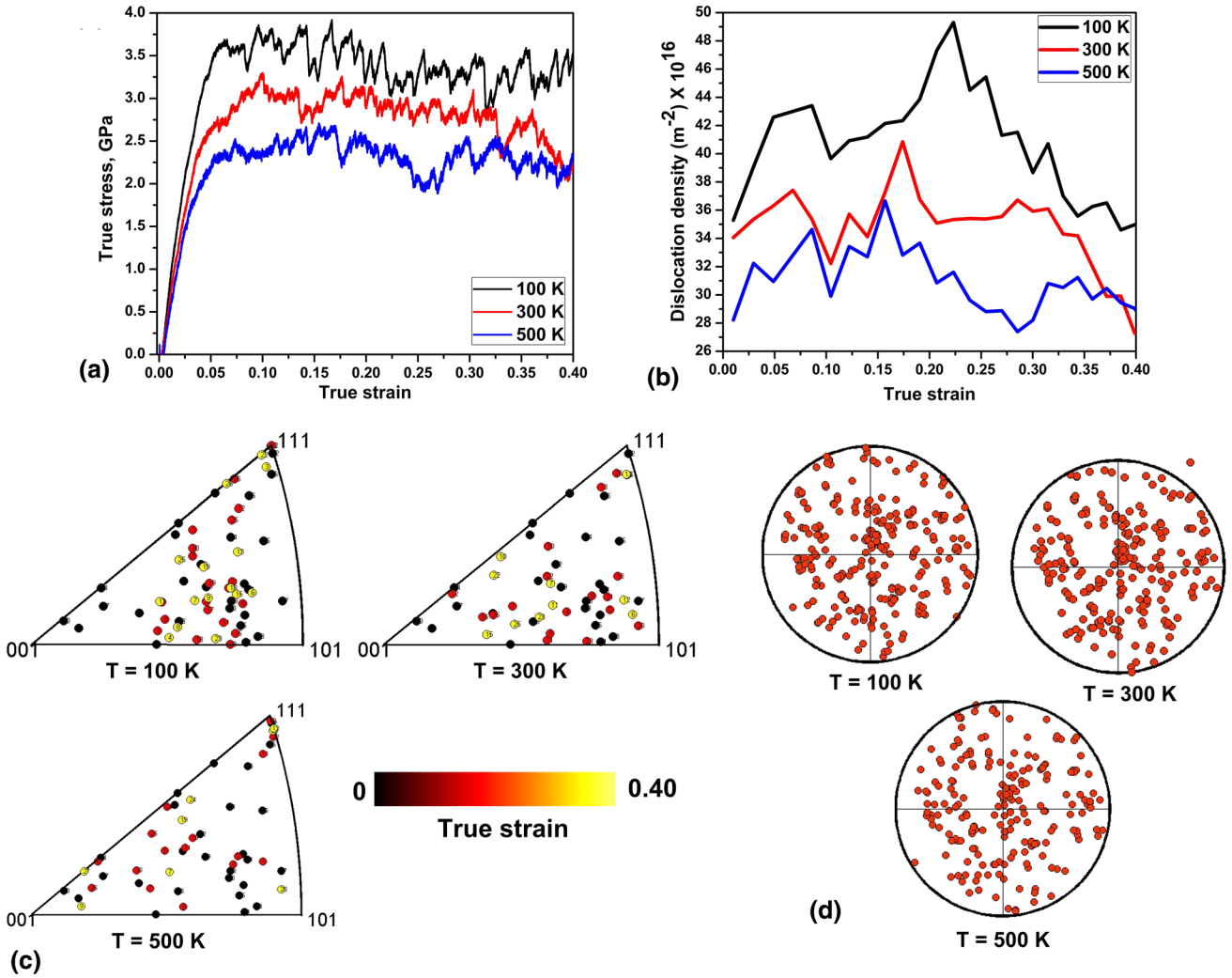

Fig. 3 (a) True tensile stress–strain curves at various temperatures, (b) dislocation density vs. true strain plots for different temperatures under tensile test, (c) inverse pole stereographic projections along Z-direction show the evolution of the orientations of overall random texture distribution of all grains for different temperatures during tensile deformation test and (d) pole figures represent overall random texture distribution of grain orientation {111} type pole in the specimens at different temperatures taken at 40% of true strains under tensile deformations condition

Atomic strain snapshots of NC Ni having grain size ~ 5 nm after different cycles of ratcheting at 500 K and − 0.6 stress ratio are presented in Fig. 5. It is observed that with the increase in ratcheting cycle, shear strains increased at the initial stage of ratcheting cycle. After first cycle of ratcheting strain, shear strains are found to be remained almost unchanged with the increasing number of loading cycles. Shear strains are found to be mainly localized at the grain boundaries (GBs). It is because of the local stress concentrations, which are generated mainly at GBs compared to grains (refer to Fig. 5). It is found from Fig. 4 and 5 that ratcheting strain and shear strains both are almost remained unaltered from the first cycle to the sixth cycle with the increasing number of asymmetrical cycles. It can be said that shear strains supported the behavior of ratcheting strain curves. Figure 6 depicts the atomic strain snapshots of NC Ni after completed the sixth ratcheting cycle at three different temperatures (100, 300 and 500 K) and $R = -0.6$ stress ratio. It is observed from Fig. 6 that shear strains increased with the increasing temperature under asymmetrical cyclic loading condition. It is found from Fig. 4 and 6 that ratcheting strain and shear strain both increased with the increasing temperature during the deformation process under asymmetric cyclic loading.

Cluster analysis has been performed taking the cutoff radius as 2.48 Å to study the structural evolution by considering the local atomic configurations during asymmetric cyclic loading. The number of clusters with respect to the number of loading cycles for different temperatures at specific stress ratios is plotted in Fig. 7(a), (b) and (c). The number of clusters decreases with the increasing deformation temperature, which indicates that formation of amorphous structure is started during asymmetric cyclic loading. It can be observed that the number of clusters rises sharply at every first half cycle during the tensile loading and decreases during the compressive loading and the same trend is repeated up to six cycles. The increase in the number of clusters implies reduction in crystallinity, and the same is happened due to the formation of amorphous structure. Figure 7(d), (e) and (f) shows that stress ratio does not show any significant effect on the number of clusters during ratcheting. In fact, there is hardly any effect

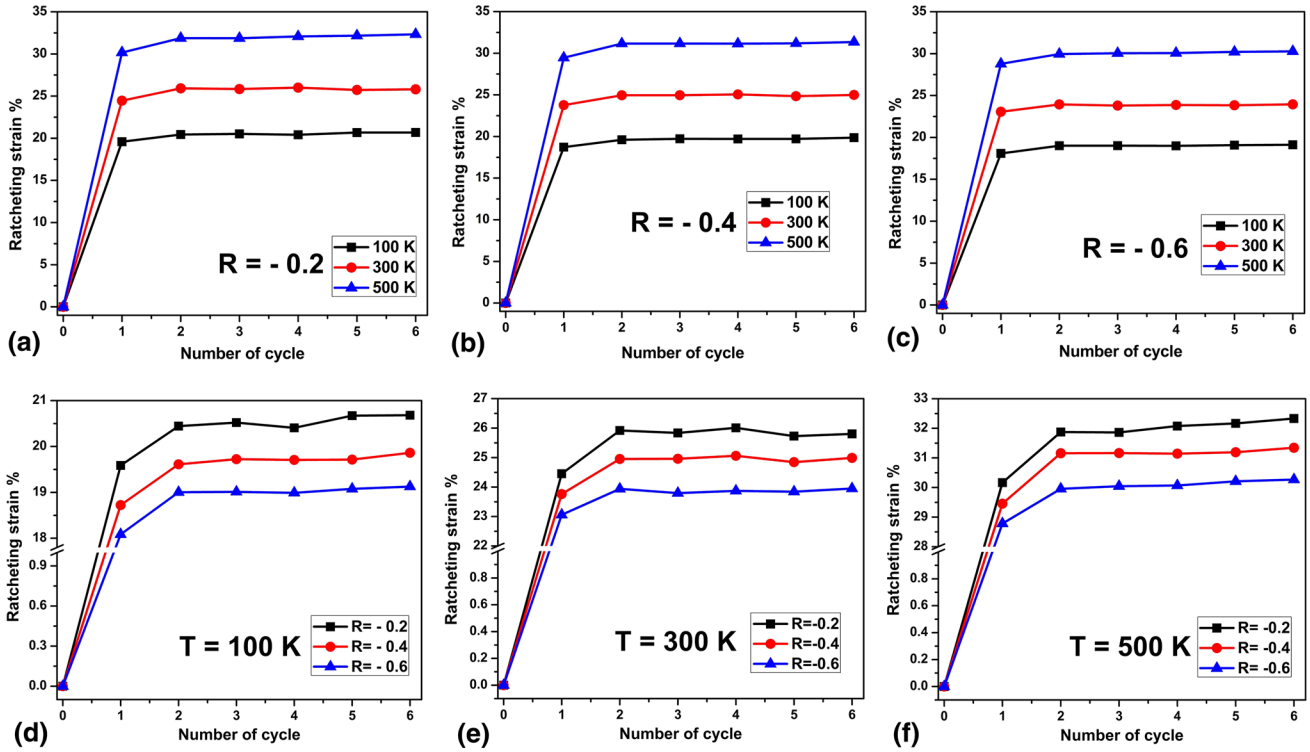

Fig. 4 Ratcheting strain vs. number of cycles for various temperatures for specific stress ratios such as (a) $R = -0.2$, (b) $R = -0.4$ and (c) $R = -0.6$ and various stress ratios (R) for specific temperatures such as (d) 100 K, (e) 300 K, (f) 500 K

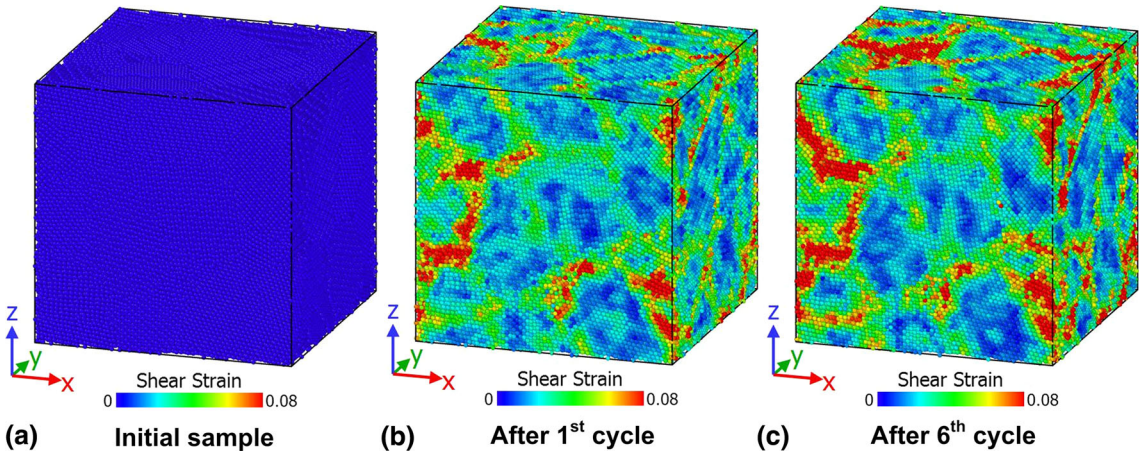

Fig. 5 Atomic configuration snapshots of NC Ni during ratcheting cycle such as (a) initial sample, (b) after the completion of the first cycle and (c) after the completion of the sixth cycle at $R = -0.6$ and $T = 500$ K

of change in stress ratio on structural evolution in ultrafine-grained NC Ni during ratcheting.

Variation in vacancies with respect to the number of cycles for different stress ratios and different temperatures during the asymmetric cyclic loading is shown in Fig. 8 (a), (b) and (c). It has been observed that with the increase in temperature the curves shifted upwards. As we know that concentration of vacancies strongly depends on temperature, and with the increase in temperature equilibrium concentration of vacancies increases during ratcheting test. It is observed that the number of vacancies during compressive part of loading cycle becomes stationary at 100 and 300 K deformation temperatures. It is because both applied compressive stress and deformation temperatures are low (i.e., 100 and 300 K). While at higher deformation temperature (i.e., 500 K) for same compressive stress, the variation in the number of vacancies is exhibited (refer to Fig. 8a, b, and c). Figure 7(d), (e) and (f) shows that the number of vacancies rises to sharp peak at each midpoint of every half cycle during the tensile loading which induces strain in the specimen and during relaxation vacancies comes to their equilibrium concentration followed by compression cycle and the number of vacancies almost remains constant. It has been observed that stress ratio does not show any considerable impact on vacancy concentration, indicating that there is no effect of variation in stress ratio on structural evolution in ultrafine-grained NC Ni specimen at various temperatures, viz.

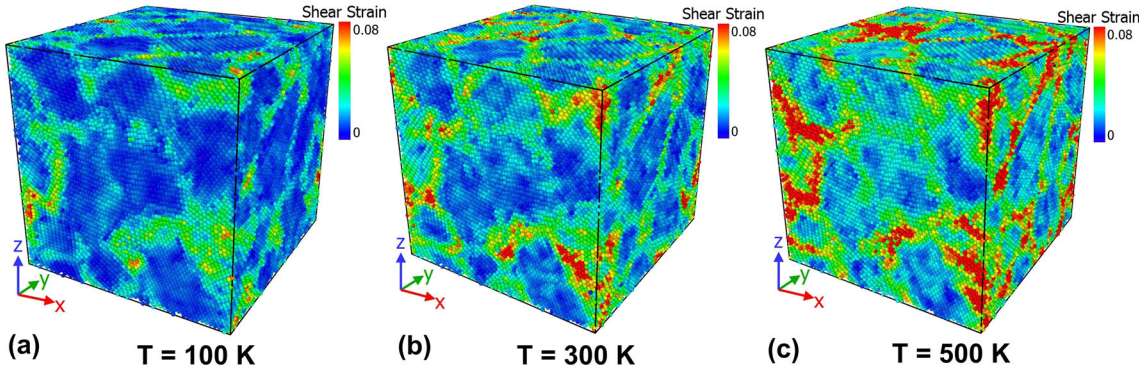

Fig. 6 Atomic configuration snapshots of NC Ni after the completion of the sixth cycle for (a) 100 K, (b) 300 K and (c) 500 K temperature at $R = -0.6$

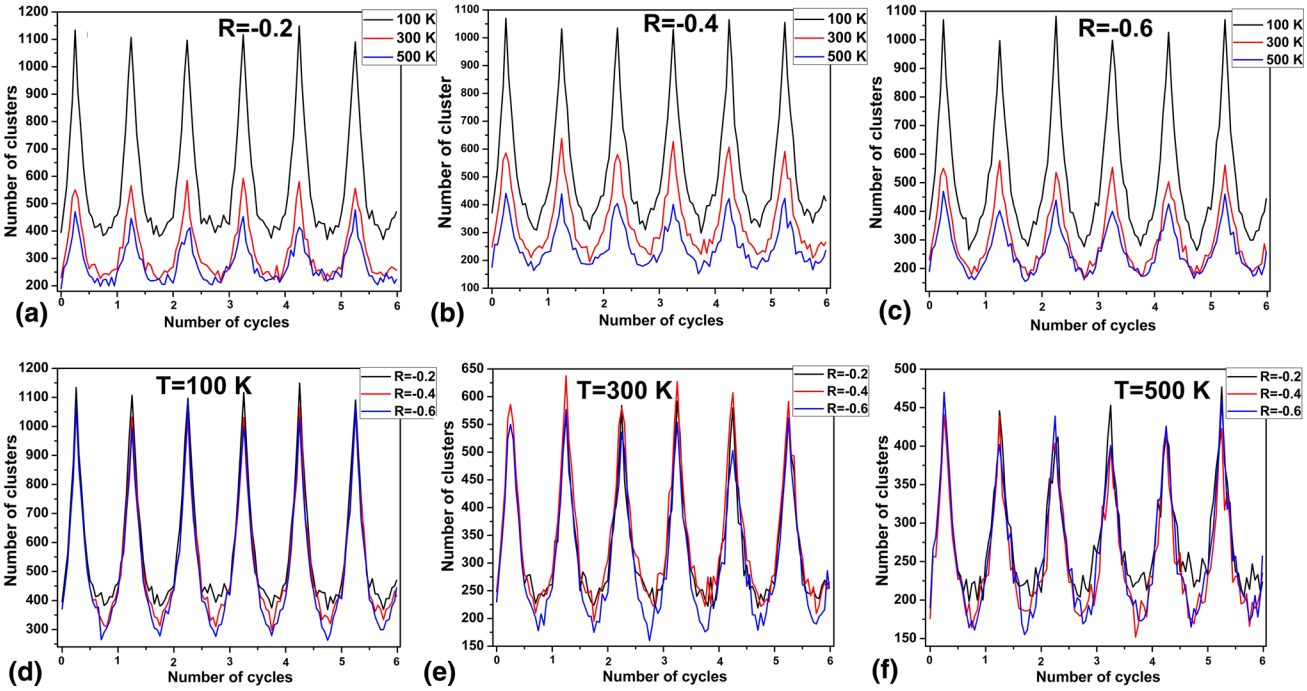

Fig. 7 Number of clusters vs. number of cycles for various temperatures, at stress ratio of (a) $R = -0.2$, (b) $R = -0.4$, (c) $R = -0.6$ and various stress ratios (R), at temperature of (d) 100 K, (e) 300 K and (f) 500 K

100, 300, 500 K, for different stress ratios (R) such as − 0.2, − 0.4 and − 0.6, respectively. During the ratcheting deformation process, after each and every cycle the vacancy concentration increases slightly which implies accumulation of plastic strain in the material.

Variation in dislocation density with the number of cycles has been determined for different temperatures at specific stress ratio as illustrated in Fig. 9(a), (b) and (c). It is worth being noting that the effect of variation in temperature shows significant influence on the dislocation density after six cycles of asymmetric loading as dislocations are responsible for deformation. With the increase in the temperature, the dislocation density curves are shifted downwards, which indicates that mass diffusion of atoms increases the movement of all kinds of defects and accordingly helps in annihilation of dislocations having opposite sign. Figure 9(d), (e) and (f) shows that with the increase in the stress ratio there is no considerable impact on change in dislocation density during the asymmetric cyclic loading. It has been observed that variation in dislocation density versus the number of cycles shows zigzag pattern indicating strain hardening and work softening, but the average dislocation density remains almost constant during asymmetric cyclic loading. For stress ratios $R = -0.2$, -0.4 and -0.6, with the increase in the temperature the fluctuations of dislocation density gradually decrease and may be attributed to dynamic recovery during the ratcheting.

Figure 10(a), (b) and (c) shows the inverse pole figure at different temperatures with grains labeled for the number of cycles. It is known that inverse pole figures give information about the orientation of grains in specimen with respect to reference of crystallographic directions. In this study, all the grains have been tracked using GTA and track changes to their orientation as function of the number of cycles at three different temperatures. It has been observed that with the increase in temperature there is a slight change in the grain rotation

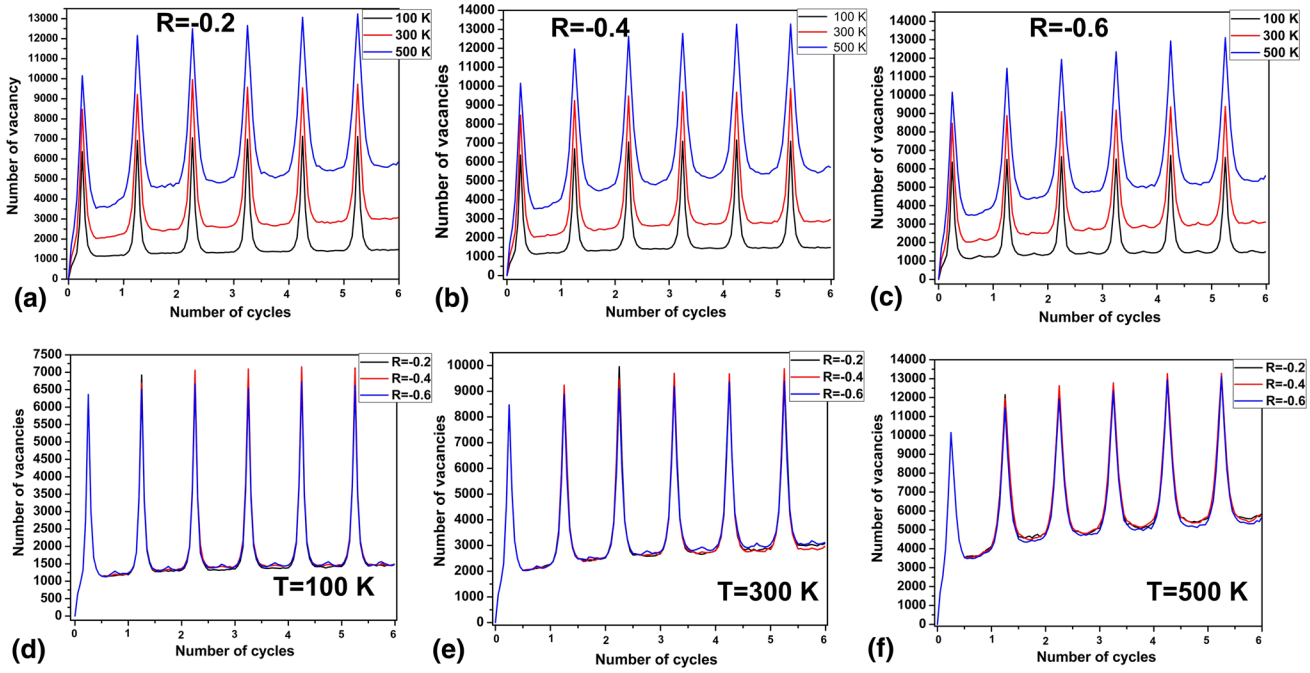

Fig. 8 Number of vacancies vs. number of cycles for various temperatures, at stress ratio of (a) $R = -0.2$, (b) $R = -0.4$, (c) $R = -0.6$ and various stress ratios (R), at temperature of (d) 100 K, (e) 300 K and (f) 500 K

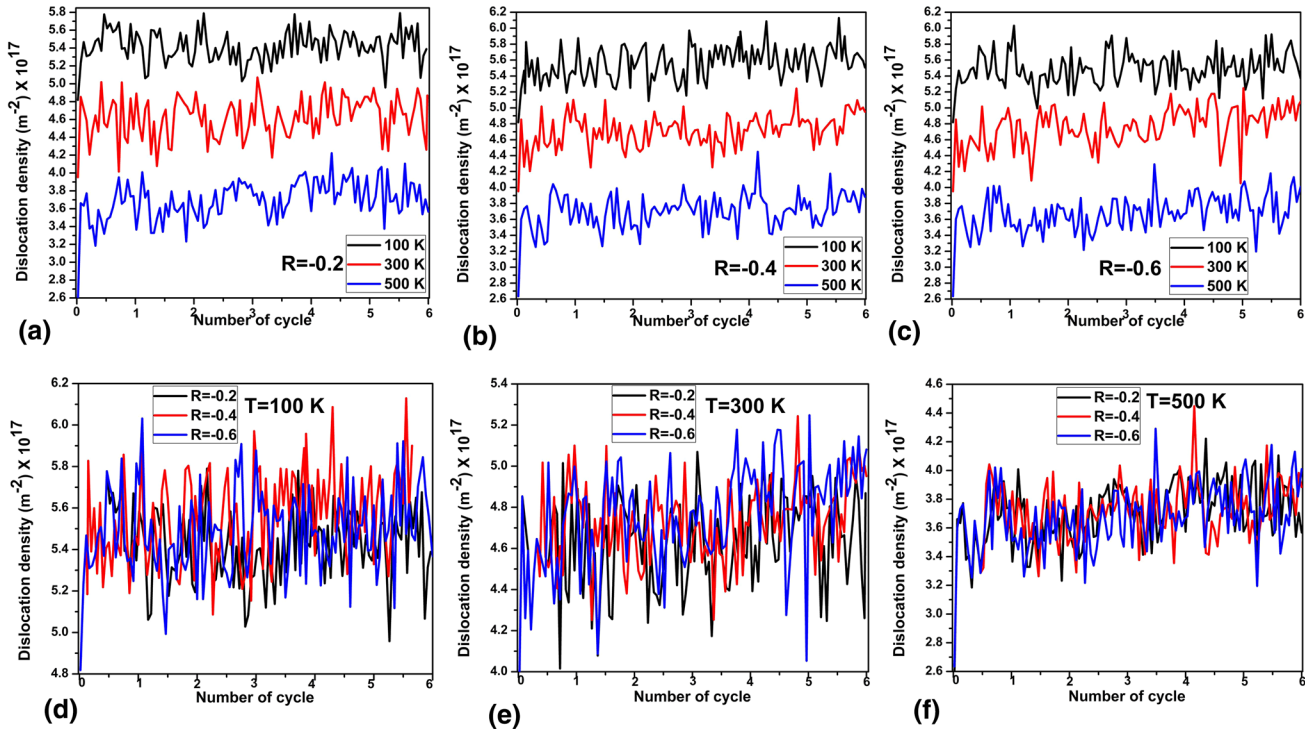

Fig. 9 Dislocation density vs. number of cycles for various temperatures, at stress ratio of (a) $R = -0.2$, (b) $R = -0.4$, (c) $R = -0.6$ and various stress ratios (R), at temperature of (d) 100 K, (e) 300 K and (f) 500 K

because of increased diffusion at such high temperature and the same can be identified by displacement of each point during asymmetric cyclic loading at 300 and 500 K. It has been observed that rotation of the some of the grains is likely to be limited which may be due to dependence on compatibility with surrounding atoms and its orientation is strongly dependent on temperature (Ref 56). It may be well related with the experimental findings that grain rotation changes at elevated temperatures by changing the atomic positions at the grain boundaries and reported that grain rotation depends on the net force acting on the grain and diffusion along the grain boundaries (Ref 48, 57, 58).

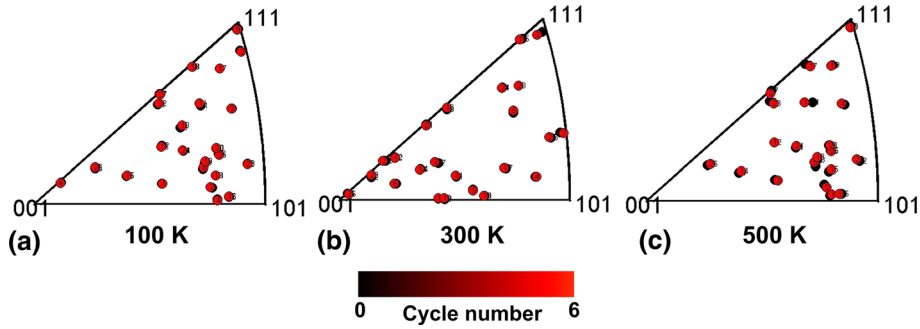

Fig. 10 *Z*-direction inverse pole stereographic projections show the evolution of the orientations of overall random texture distribution of all grains at each temperature after the completion of cycle 6

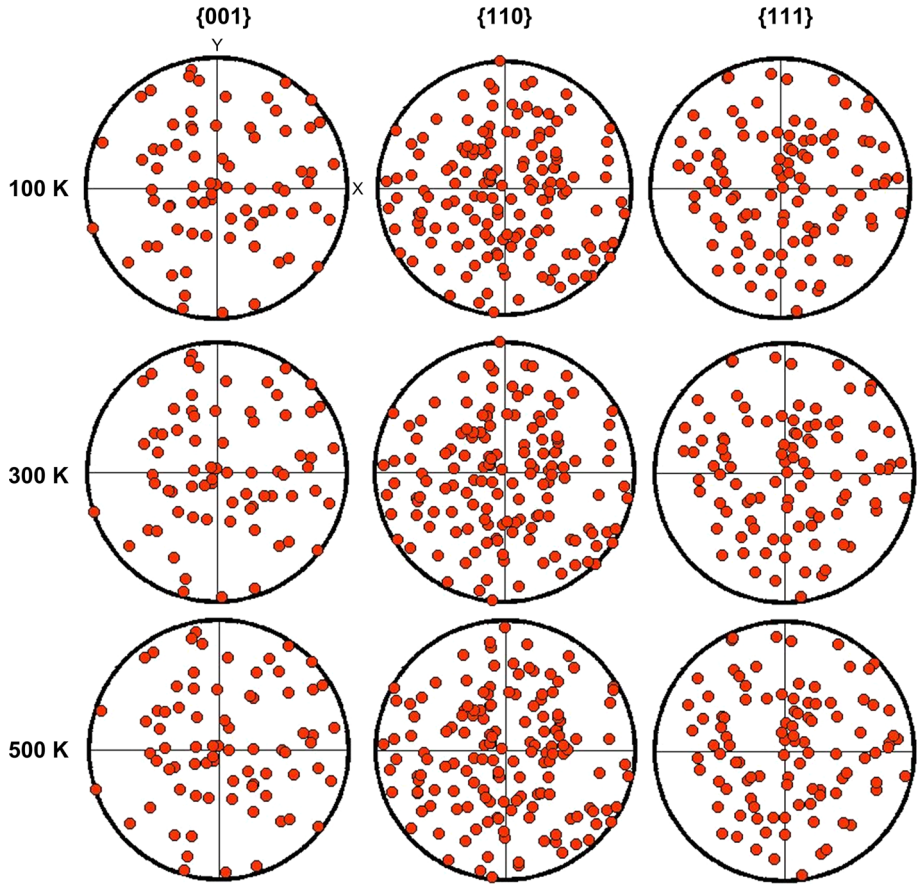

Fig. 11 Pole figure represents of overall random texture distribution in the specimens at three different temperatures, viz. 100, 300 and 500 K, taken after the completion of cycle 6

Figure 11 shows that pole figure distributions for {100}, {110} and {111} at temperatures, viz. 100, 300 and 500 K. It has been observed that the number of poles projected at three different temperatures remains almost same, and it can be inferred from the above that there is no significant change in the final texture evolved during the ratcheting.

After ratcheting, certain amount of plastic strain accommodated may damage the material. In order to understand the effect of ratcheting, post-tensile tests have been carried out for different stress ratios such as $R = -0.2$, -0.4 and -0.6 at three different temperatures, viz. 100, 300 and 500 K, respectively. To analyze the mechanical response, engineering stress–strain curves are plotted in Fig. 12(a), (b) and (c). It has been observed that with the increase in temperature at specific stress ratio the curves shifted downwards which implies that the sample has lower strength at high temperature. On the other hand, variation in stress ratio on stress–strain curves at particular temperature is plotted in Fig. 12(d), (e) and (f). It can be clearly noticed that stress ratio hardly shows any effect after ratcheting during the deformation. It can be inferred from the above that obtained stress–strain curves are more temperature sensitive compared to stress ratio during the deformation. Figure 12(g) shows ultimate tensile strength (UTS) versus temperature at different stress ratios after ratcheting which clearly indicates that UTS remains same. It may be due to no change in average dislocation density.

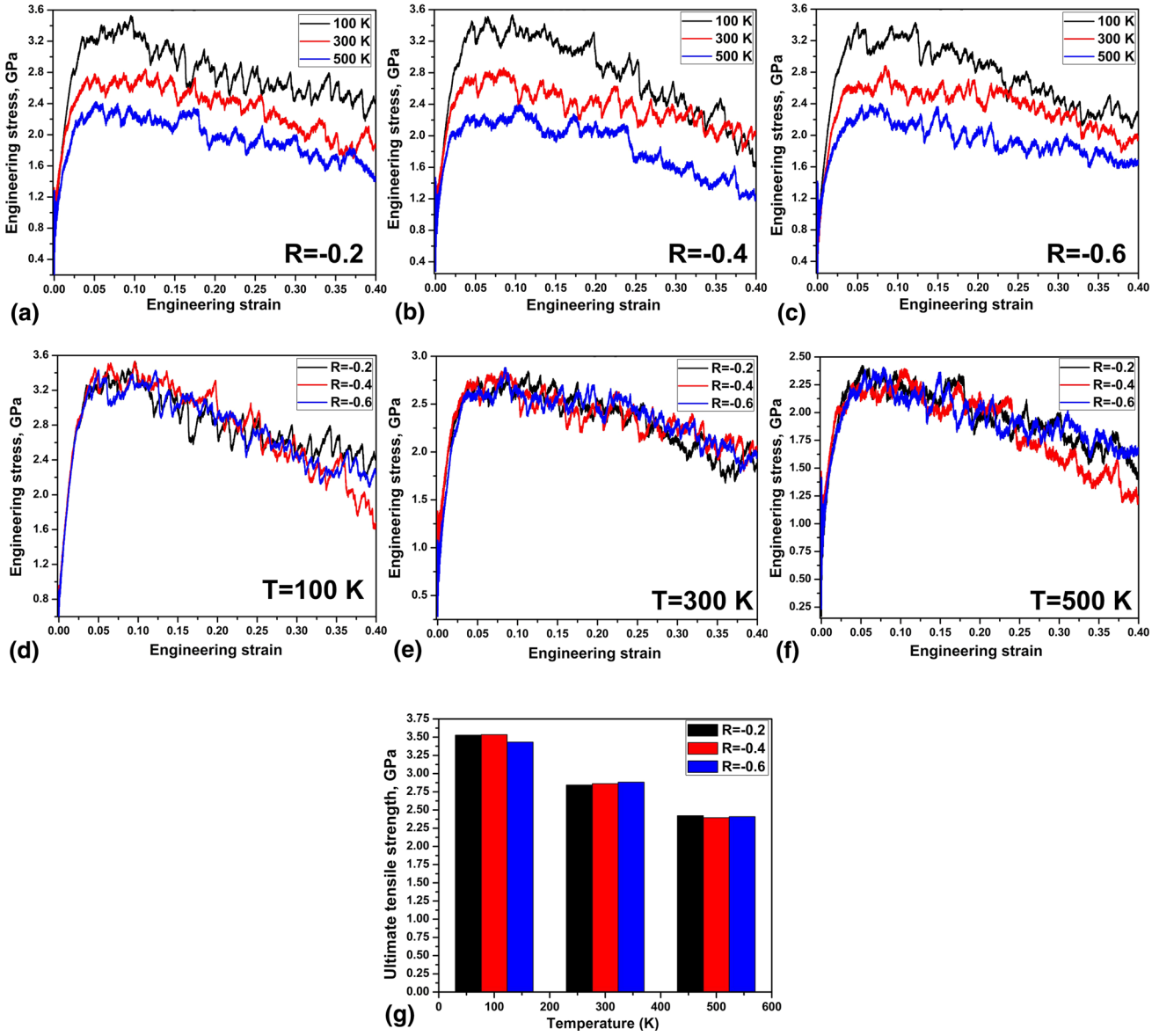

Fig. 12 Post-ratcheting tensile stress–strain curves for various temperatures, at stress ratio of (a) $R = -0.2$, (b) $R = -0.4$, (c) $R = -0.6$ and various stress ratios (R), at temperature of (d) 100 K, (e) 300 K, (f) 500 K and (g) post-ratcheting tensile strength vs. temperature

4. Conclusions

Ratcheting behavior of NC Ni is studied at different temperatures, viz. 100, 300 and 500 K, for different stress ratios such as $R = -0.2$, -0.4 and -0.6 using molecular dynamics simulation. The significant increase in ratcheting strain has been observed with the increase in test temperature. Slight reduction in crystallinity has been observed at every first half loading cycle from the performed cluster analysis. With the increase in temperature, the number of vacancies increases, the number of clusters decreases, zigzag pattern of dislocation density has been observed while NC Ni specimen is subjected to asymmetric cyclic loading condition. Stress ratio does not show any significant impact on structural evolution during ratcheting deformation process. It can be inferred that temperature is more influential factor than stress ratio on structural evolution in ultrafine-grained NC Ni. Slight change in grain rotation has been observed with the increase in temperature, and from the pole figures there is no significant change in the final texture evolved at different temperatures during ratcheting test. UTS remains same for NC Ni specimen before and after simulated ratcheting deformation process, which may be due to repetitive strain hardening and work softening phenomenon as evident from dislocation density plots. This work will be helpful to conceptualize the ratcheting of pure NC Ni, and collection of this work can be extended to study the effect of controlling parameters in multicomponent alloy nanocrystalline metallic system and its underlying deformation mechanism along with structural changes under asymmetric cyclic loading condition.

References

1. B.S. Murty, P. Shankar, B. Raj, B.B. Rath, and J. Murday, *Textbook of Nanoscience and Nanotechnology*, Springer, Berlin, 2013

2. R. Kelsall, I.W. Hamley, and M. Geoghegan, Ed., *Nanoscale Science and Technology*, Wiley, Hoboken, 2005
3. H. Gleiter, Nanostructured Materials: Basic Concepts and Microstructure, *Acta Mater.*, 2000, **48**(1), p 1–29
4. S. Pal, M. Meraj, and C. Deng, Effect of Zr Addition on Creep Properties of Ultra-fine Grained Nanocrystalline Ni Studied by Molecular Dynamics Simulations, *Comput. Mater. Sci.*, 2017, **126**, p 382–392
5. H.S. Kim and Y. Estrin, Strength and Strain Hardening of Nanocrystalline Materials, *Mater. Sci. Eng. A*, 2008, **483**, p 127–130
6. B.T.F. Tang, U. Erb, and I. Brooks, Strain Hardening in Polycrystalline and Nanocrystalline Nickel, *Adv. Mater. Res.*, 2012, **409**, p 550–554
7. K.S. Kumar, S. Suresh, M.F. Chisholm, J.A. Horton, and P. Wang, Deformation of Electrodeposited Nanocrystalline Nickel, *Acta Mater.*, 2013, **51**(2), p 387–405
8. T.J. Rupert, D.S. Gianola, Y. Gan, and K.J. Hemker, Experimental observations of stress-driven grain boundary migration, *Science*, 2009, **326**(5960), p 1686–1690
9. M. Ke, S.A. Hackney, W.W. Milligan, and E.C. Aifantis, Observation and Measurement of Grain Rotation and Plastic Strain in Nanostructured Metal Thin Films, *Nanostruct. Mater.*, 1995, **5**(6), p 689–697
10. Z. Shan, E.A. Stach, J.M.K. Wiezorek, J.A. Knapp, D.M. Follstaedt, and S.X. Mao, Grain Boundary-Mediated Plasticity in Nanocrystalline Nickel, *Science*, 2004, **305**(5684), p 654–657
11. H. Van Swygenhoven and P.M. Derlet, Grain-Boundary Sliding in Nanocrystalline fcc Metals, *Phys. Rev. B*, 2001, **64**(22), p 224105
12. A. Pineau, A.A. Benzerga, and T. Pardoen, Failure of Metals III: Fracture and Fatigue of Nanostructured Metallic Materials, *Acta Mater.*, 2016, **107**, p 508–544
13. K.S. Kumar, H. Van Swygenhoven, and S. Suresh, Mechanical Behavior of Nanocrystalline Metals and Alloys, *Acta Mater.*, 2003, **51**(19), p 5743–5774
14. M. Dao, L. Lu, R.J. Asaro, J.T.M. De Hosson, and E. Ma, Toward a Quantitative Understanding of Mechanical Behavior of Nanocrystalline Metals, *Acta Mater.*, 2007, **55**(12), p 4041–4065
15. K.S. Siow, A.A.O. Tay, and P. Oruganti, Mechanical Properties of Nanocrystalline Copper and Nickel, *Mater. Sci. Technol.*, 2004, **20**(3), p 285–294
16. H. Van Swygenhoven, P.M. Derlet, and A. Hasnaoui, Atomic Mechanism for Dislocation Emission from Nanosized Grain Boundaries, *Phys. Rev. B*, 2002, **66**(2), p 024101
17. A. Cao and Y. Wei, Atomistic Simulations of Crack Nucleation and Intergranular Fracture in Bulk Nanocrystalline Nickel, *Phys. Rev. B*, 2007, **76**(2), p 024113
18. T. Hanlon, E.D. Tabachnikova, and S. Suresh, Fatigue Behavior of Nanocrystalline Metals and Alloys, *Int. J. Fatigue*, 2005, **27**(10–12), p 1147–1158
19. Z. Xia, D. Kujawski, and F. Ellyin, Effect of Mean Stress and Ratcheting Strain on Fatigue Life of Steel, *Int. J. Fatigue*, 1996, **18**(5), p 335–341
20. S.K. Paul, S. Sivaprasad, S. Dhar, and S. Tarafder, Cyclic Plastic Deformation and Cyclic Hardening/Softening Behavior in 304LN Stainless Steel, *Theor. Appl. Fract. Mech.*, 2010, **54**(1), p 63–70
21. Y. Jiang and H. Sehitoglu, Cyclic Ratcheting of 1070 Steel Under Multiaxial Stress States, *Int. J. Plast.*, 1994, **10**(5), p 579–608
22. T. Hassan and S. Kyriakides, Ratcheting of Cyclically Hardening and Softening Materials: I. Uniaxial Behavior, *Int. J. Plast.*, 1994, **10**(2), p 149–184
23. X. Yang, Low Cycle Fatigue and Cyclic Stress Ratcheting Failure Behavior of Carbon Steel 45 Under Uniaxial Cyclic Loading, *Int. J. Fatigue*, 2005, **27**(9), p 1124–1132
24. C.B. Lim, K.S. Kim, and J.B. Seong, Ratcheting and Fatigue Behavior of a Copper Alloy Under Uniaxial Cyclic Loading with Mean Stress, *Int. J. Fatigue*, 2009, **31**(3), p 501–507
25. G. Kang, Y. Liu, J. Ding, and Q. Gao, Uniaxial Ratcheting and Fatigue Failure of Tempered 42CrMo Steel: Damage Evolution and Damage-Coupled Visco-Plastic Constitutive Model, *Int. J. Plast.*, 2009, **25**(5), p 838–860
26. G. Chen, X. Chen, and C.D. Niu, Uniaxial Ratcheting Behavior of 63Sn37Pb Solder with Loading Histories and Stress Rates, *Mater. Sci. Eng. A*, 2006, **421**(1–2), p 238–244
27. G.Z. Kang, Y.G. Li, J. Zhang, Y.F. Sun, and Q. Gao, Uniaxial Ratcheting and Failure Behaviors of Two Steels, *Theor. Appl. Fract. Mech.*, 2005, **43**(2), p 199–209
28. W.J. Chang and T.H. Fang, Influence of Temperature on Tensile and Fatigue Behavior of Nanoscale Copper Using Molecular Dynamics Simulation, *J. Phys. Chem. Solids*, 2003, **64**(8), p 1279–1283
29. J.F. Panzarino, J.J. Ramos, and T.J. Rupert, Quantitative Tracking of Grain Structure Evolution in a Nanocrystalline Metal During Cyclic Loading, *Model. Simul. Mater. Sci. Eng.*, 2015, **23**(2), p 025005
30. J. Schiøtz, Strain-Induced Coarsening in Nanocrystalline Metals Under Cyclic Deformation, *Mater. Sci. Eng. A*, 2004, **375**, p 975–979
31. D. Farkas, M. Willemann, and B. Hyde, Atomistic Mechanisms of Fatigue in Nanocrystalline Metals, *Phys. Rev. Lett.*, 2005, **94**(16), p 165502
32. T.J. Rupert and C.A. Schuh, Mechanically Driven Grain Boundary Relaxation: A Mechanism for Cyclic Hardening in Nanocrystalline Ni, *Philos. Mag. Lett.*, 2012, **92**(1), p 20–28
33. W.J. Chang, Molecular-Dynamics Study of Mechanical Properties of Nanoscale Copper with Vacancies Under Static and Cyclic Loading, *Microelectron. Eng.*, 2003, **65**(1–2), p 239–246
34. B. Moser, T. Hanlon, K.S. Kumar, and S. Suresh, Cyclic Strain Hardening of Nanocrystalline Nickel, *Scr. Mater.*, 2006, **54**(6), p 1151–1155
35. D. Chen, Structural Modeling of Nanocrystalline Materials, *Comput. Mater. Sci.*, 1995, **3**(3), p 327–333
36. J. Li, AtomEye: An Efficient Atomistic Configuration Viewer, *Model. Simul. Mater. Sci. Eng.*, 2003, **11**(2), p 173
37. Z. Shao, N. Li, J. Lin, and T.A. Dean, Strain Measurement and Error Analysis in Thermo-Mechanical Tensile Tests of Sheet Metals for Hot Stamping Applications, *Proc. Inst. Mech. Eng. Part C Mech. Eng. Sci.*, 2018, **232**(11), p 1994–2008
38. H. Bei, S. Shim, G.M. Pharr, and E.P. George, Effects of Pre-strain on the Compressive Stress–Strain Response of Mo-Alloy Single-Crystal Micropillars, *Acta Mater.*, 2008, **56**(17), p 4762–4770
39. X. Yang, Low Cycle Fatigue and Cyclic Stress Ratcheting Failure Behavior of Carbon Steel 45 Under Uniaxial Cyclic Loading, *Int. J. Fatigue*, 2005, **27**(9), p 1124–1132
40. J. Jabra, M. Romios, J. Lai, E. Lee, M. Setiawan, J.R. Ogren, and N. Abourialy, The Effect of Thermal Exposure on the Mechanical Properties of 2099-T6 Die Forgings, 2099-T83 Extrusions, 7075-T7651 Plate, 7085-T7452 Die Forgings, 7085-T7651 Plate, and 2397-T87 Plate Aluminum Alloys, *J. Mater. Eng. Perform.*, 2006, **15**(5), p 601–607
41. H.J. Berendsen, J.V. Postma, W.F. van Gunsteren, A.R.H.J. DiNola, and J.R. Haak, Molecular Dynamics with Coupling to an External Bath, *J. Chem. Phys.*, 1984, **81**(8), p 3684–3690
42. S. Plimpton, Fast Parallel Algorithms for Short-Range Molecular Dynamics, *J. Comput. Phys.*, 1995, **117**(1), p 1–19
43. M.I. Mendelev, M.J. Kramer, S.G. Hao, K.M. Ho, and C.Z. Wang, Development of Interatomic Potentials Appropriate for Simulation of Liquid and Glass Properties of $NiZr_2$ Alloy, *Philos. Mag.*, 2012, **92**(35), p 4454–4469
44. M. Meraj and S. Pal, Nano-scale Simulation Based Study of Creep Behavior of Bimodal Nanocrystalline Face Centered Cubic Metal, *J. Mol. Model.*, 2017, **23**(11), p 309
45. B. von Blanckenhagen, E. Arzt, and P. Gumbsch, Discrete Dislocation Simulation of Plastic Deformation in Metal Thin Films, *Acta Mater.*, 2004, **52**(3), p 773–784
46. N. Juslin, V. Jansson, and K. Nordlund, Simulation of Cascades in Tungsten-Helium, *Philos. Mag.*, 2010, **90**(26), p 3581–3589
47. K. Nordlund, M. Ghaly, R.S. Averback, M. Caturla, T.D. de La Rubia, and J. Tarus, Defect Production in Collision Cascades in Elemental Semiconductors and fcc Metals, *Phys. Rev. B*, 1998, **57**(13), p 7556
48. C.L. Kelchner, S.J. Plimpton, and J.C. Hamilton, Dislocation Nucleation and Defect Structure during Surface Indentation, *Phys. Rev. B*, 1998, **58**(17), p 11085
49. J.C. Zhang, C. Chen, Q.X. Pei, Q. Wan, W.X. Zhang, and Z.D. Sha, Ab Initio Molecular Dynamics Study of the Local Atomic Structures in Monatomic Metallic Liquid and Glass, *Mater. Des.*, 2015, **77**, p 1–5
50. D. Faken and H. Jónsson, Systematic Analysis of Local Atomic Structure Combined with 3D Computer Graphics, *Comput. Mater. Sci.*, 1994, **2**(2), p 279–286
51. A. Stukowski, Visualization and Analysis of Atomistic Simulation Data with OVITO–The Open Visualization Tool, *Model. Simul. Mater. Sci. Eng.*, 2009, **18**(1), p 015012
52. J.F. Panzarino and T.J. Rupert, Tracking Microstructure of Crystalline Materials: A Post-processing Algorithm for Atomistic Simulations, *JOM*, 2014, **66**(3), p 417–428

53. Z. Budrovic, H. Van Swygenhoven, P.M. Derlet, S. Van Petegem, and B. Schmitt, Plastic Deformation with Reversible Peak Broadening in Nanocrystalline Nickel, *Science*, 2004, **304**(5668), p 273–276
54. M. Meraj, N. Yedla, and S. Pal, Role of W on the Dislocation Evolution in Ni-W Alloy during Tension Followed by Compression Loading, *Met. Mater. Int.*, 2016, **22**(3), p 373–382
55. F. Panzarino, Quantification of Grain Boundary Mediated Plasticity Mechanisms in Nanocrystalline Metals, Doctoral Dissertation, UC Irvine, 2016
56. M.F. Ashby and R.A. Verrall, Diffusion-Accommodated Flow and Superplasticity, *Acta Metall.*, 1973, **21**(2), p 149–163
57. K.E. Harris, V.V. Singh, and A.H. King, Grain Rotation in Thin Films of Gold, *Acta Mater.*, 1998, **46**(8), p 2623–2633
58. M.Y. Gutkin, I.A. Ovidko, and N.V. Skiba, Crossover from Grain Boundary Sliding to Rotational Deformation in Nanocrystalline Materials, *Acta Mater.*, 2003, **51**(14), p 4059–4071